New Elastica Geodesic Approach with Convexity Shape Prior for Region-based Active Contours and Image Segmentation

Da Chen, Laurent Cohen, Jean-Marie Mirebeau, Xue-Cheng Tai

New Elastica Geodesic Approach with Convexity Shape Prior for Region-based Active Contours and Image Segmentation

Da Chen
Shandong Artificial Intelligence Institute,
Qilu University of Technology
(Shandong Academy of Sciences), China
dachen.cn@hotmail.com

Jean-Marie Mirebeau
Laboratoire de mathématiques d'Orsay,
CNRS, Université Paris-Sud, Université Paris-Saclay,
91405 ORSAY, France
jean-marie.mirebeau@math.u-psud.fr

Xue-Cheng Tai
Department of Mathematics,
Hong Kong Baptist University, Kowloon Tong,
Hong Kong
xuechengtai@hkbu.edu.hk

Laurent D. Cohen
University Paris Dauphine,
PSL Research University, CNRS,
UMR 7534, CEREMADE, 75016 Paris, France.
cohen@ceremade.dauphine.fr

March 18, 2021

Abstract

The minimal geodesic models based on the Eikonal equations are capable of finding suitable solutions in various image segmentation scenarios. Currently, existing geodesic-based segmentation approaches usually exploit the image features in conjunction with regularization terms, such as curve length, for computing geodesic paths. In this paper, we consider a more complicated problem: finding simple closed geodesic curves which are imposed a convexity shape prior. The proposed approach relies on an orientation-lifting strategy, by which a planar curve can be mapped to an high-dimensional orientation space. The convexity shape priors serve as a constraint for the construction of local metrics in the lifted space. The geodesic curves then can be efficiently computed through the single-pass Fast Marching method (FMM). In addition, we introduce a way to incorporate region-based homogeneity features into the proposed geodesic model so as to solve the region-based segmentation issues with

shape prior constraints.

1 Introduction

Image segmentation is a fundamental and challenging problem posed in the fields of image analysis and computer vision. In the past decades, a large variety of segmentation approaches have been devoted to address such a problem. Among them, the energy minimization-based models integrating with priors on the target regions have proven to yield satisfactory solutions in many segmentation scenarios.

Prior-driven segmentation approaches. One widely considered geometric prior is to assume that the target boundaries appear to be short in terms of Euclidean curve length, by which the image noises can be suppressed in some extent. Such a geometric prior has been commonly exploited for segmentation in various energy minimization-based segmentation approaches such as active contours [9, 10, 36] and graph-based models [5, 26]. Efficient variants of the Euclidean length-based geometric prior might include curvature-penalized length term [3, 23, 41] and edge-based weighted length [30, 40]. However, utilizing geometric regularity as a single prior is sometimes insufficient to find favorable segmentation results, especially when dealing with images with complex gray level distribution. In contrast, the strategy of incorporating shape-driven priors into the objective energies is able to yield more accurate and efficient constraints for segmentation. These priors are often carried out via a statistical model about the target regions or contours [6, 8, 19, 20, 38]. The implementation of the shape-driven priors is capable of encouraging satisfactory segmentations, even in the absence of reliable image appearance features which are used to distinguish disjoint regions.

Recently, the constraints of convexity and star convexity were introduced as flexible shape priors. Basically, existing approaches in conjunction with these shape priors can be loosely categorized as either discrete or continuous types. In the discrete setting, the convexity prior [25], the star convexity prior [44], or geodesic star convexity [27] are characterized as a regularization term to construct the discrete energy functionals together with image data-driven terms. The energy minimization can be addressed by the graph cut algorithm [5]. In [24, 39], the convexity prior was incorporated into graph-based segmentation framework to solve multi-region segmentation tasks. The hedgehog-like shape prior [29] generalizes the geodesic star convexity constraint [24] to enlarge the applicable scope of the original case. Isack *et al.* [28] proposed a flexible k-convexity prior-based model which allows overlaps between different regions. However, these graph-based approaches with convexity constraint did not consider curvature regularization.

In the continuous setting, the convexity prior is usually exploited in the active contours approaches [31, 45, 46] based on the level set formulation [37]. To be specific, in [46] the sign of the curvature was used to penalize the concave portion of the evolving contour implicitly represented by a level set function. While in [31, 45], the authors established the relationship between the Laplacian of a level set function and the convexity property of its zero-level lines, where the shape prior redefines the searching space for optimal curve. Bae *et al.* [3] illustrated that minimizing an energy regularized by a L^1-variant of Euler elastica length, which serves as a regularization term, is able to encourage the final segmentation shape to be convex. However, the convexity prior in this model is regarded as a way of implicit constraint, which heavily depends on the importance to the respective regularization term.

Geodesic active contour models. The geodesic active contour models [7, 30, 32, 47] address the edge-based segmentation problems by minimizing a weighted curve length via a gradient descent scheme. However, the local minimization scheme may lead to demanding requirement on the initialization and high sensitivity to spurious edges or noise. Cohen and Kimmel [18] proposed a minimal geodesic path model which can globally minimize a weighted curve length of isotropic metrics [7] by solving an Eikonal PDE under a given boundary condition. In this paper, we are interested in finding geodesic curves with convexity priors based on the Eikonal PDEs and Fast Marching algorithm [34]. In general, the weighted curve length along a curve with Lipschitz continuity can be measured via a local Finsler metric. Many minimal geodesic approaches have contributed to develop various Finsler metrics in order to generate suitable geodesic curves in different situations [4, 13, 17]. Chen *et al.* [12, 13] introduced an elegant way to construct Randers met-

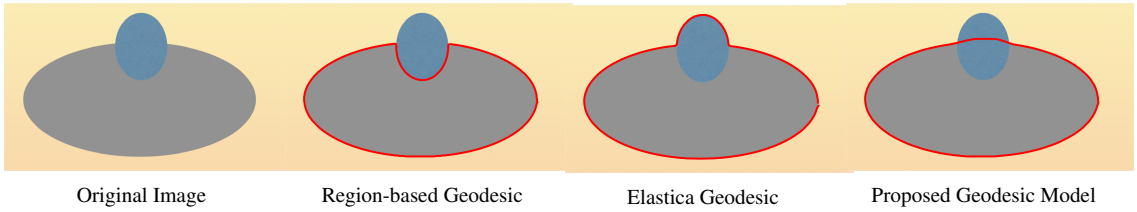

Figure 1: Image segmentation results respectively derived from the region-based region-based geodesic model, the Euler-Mumford Elastica geodesic model and the proposed elastica geodesic model with convexity constratin

rics via region-based homogeneity features, bridging the gap between the Eikonal PDEs and the region-based active contours. In [11, 16], Due to the asymmetric property, the authors exploited the asymmetric metrics for image segmentation based on the tool of Voronoi diagrams. The curvature-penalized geodesic models introduced in [14, 22] took into account an idea of orientation-lifting to address the high-order geodesic computation problems. Using suitable relaxation, geodesic distances and the geodesic paths with curvature regularization can be efficiently estimated by fast marching method [34].

Despite great advances, only the geometric priors, i.e. curve length or curvature-based length, are utilized in existing minimal geodesic approaches. In Fig. 1, we show a comparison example for geodesic curves derived from the Euler-Mumford elastica model and the proposed geodesic model [14] with convexity shape prior. In order to remove the gaps, we proposed new Eikonal PDE-based geodesic path models by integrating with curvature regularization, region-based homogeneity and convexity or star convexity priors for active contour problem, which to our best knowledge is original.

In summary, the contributions of our work are threefold:

Firstly, we introduce a new curvature-penalized minimal geodesic approach with convexity prior enhancement. The convexity restriction of geodesic curves is carried out by the signature of curvature, which is encoded into a new type of geodesic metrics established in an orientation-lifted space.

Secondly, we discuss the solutions for the computation of simple, closed and convex geodesic curves. In numerical consideration, we adopt the Hamiltonian fast marching method [34] as the numerical solver, for which the stencils are adaptively generated by the proposed geodesic metric with a convexity shape constraint.

Finally, we incorporate both region- and edge-based features into the proposed geodesic model. Accordingly, the image segmentation by the proposed model can blend the benefits from convexity prior, curvature regularization and region-based homogeneity features. Thus our model also overcomes the shortcoming of the existing curvature-penalized geodesic models [14, 22], for which only the edge-based features were used for image segmentation.

The structure of this paper is organized as follows. Section 2 gives the background on the elastica geodesic model and the Eikonal active contour model. The new elastica geodesic models with convexity shape prior are presented in Sections 3 and 4. The experimental results and the conclusion are respectively presented in Sections 5 and 6.

2 Background

Notations. Let $\mathbb{M} := \Omega \times \mathbb{S}^1$ be an orientation-lifted space, where $\Omega \subset \mathbb{R}^2$ is a bounded domain, and $\mathbb{S}^1 := \mathbb{R}/2\pi\mathbb{Z}$ can be identified with $[0, 2\pi[$ equipped with a periodic boundary condition. A point $\mathbf{x} = (x, \theta)$ is a pair comprised of a *physical* component x and an angular coordinate θ. For each $\mathbf{x} \in \mathbb{M}$, we denote by $\dot{\mathbf{x}} = (\dot{x}, \dot{\theta}) \in \mathbb{R}^2 \times \mathbb{R}$ a tangent vector at $\mathbf{x}$. In the following, we use the notation $\mathbb{E} := \mathbb{R}^2 \times \mathbb{R}$ to represent the tangent space to $\mathbb{M}$ at any base point $\mathbf{x}$. In addition, we denote by $a_+ := \max\{0, a\}$ the positive part of a real number $a \in \mathbb{R}$, and let by convention $a_+^2 := (a_+)^2$.

2.1 Euler-Mumford Geodesic Model

Orientation lifting for curvature representation. The proposed approach with convexity prior is established partially upon the curvature-penalized geodesic models [14, 22, 34]. The foundation of these models is to evaluate curvature using an orientation lifting. Consider a smooth curve $\gamma : [0,1] \to \Omega$, with non-vanishing velocity[1]. Then there exists a unique $\eta : [0,1] \to \mathbb{S}^1$ obeying for all $\varrho \in [0,1]$

$$\gamma'(\varrho) = (\cos\eta(\varrho), \sin\eta(\varrho))^T \, \|\gamma'(\varrho)\|. \tag{1}$$

In other words, $\eta(\varrho)$ encodes the tangent direction at $\gamma(\varrho)$. By Eq. (1), we define the orientation-lifted curve

$$\mathbf{\Gamma} = (\gamma, \eta) : \varrho \in [0,1] \mapsto \mathbf{\Gamma}(\varrho) \in \mathbb{M}, \tag{2}$$

whose first-order derivative is defined as $\mathbf{\Gamma}'(\varrho) = (\gamma'(\varrho), \eta'(\varrho)) \in \mathbb{E}$. In addition, the curvature $\kappa : [0,1] \to \mathbb{R}$ of the smooth curve γ is obtained as

$$\kappa(\varrho) = \eta'(\varrho) / \|\gamma'(\varrho)\|. \tag{3}$$

Euler-Mumford Elastica geodesic approach. In [14], the authors introduced a weighted curve length with curvature penality, defined as follows for a smooth curve γ

$$L^{\mathrm{EM}}(\gamma) := \int_0^1 \psi(\gamma(\varrho), \eta(\varrho)) \, (1 + \beta^2 \kappa(\varrho)^2) \|\gamma'(\varrho)\| d\varrho.$$

The parameter $\beta \in \mathbb{R}^+$ has the dimension of a radius of curvature, and modulates the strength of the curvature penalty. For simplicity, and up to a rescaling argument, we assume $\beta = 1$ in the rest of this description. The cost function $\psi : \mathbb{M} \to \mathbb{R}^+$ is orientation-dependent and derived from image gradients [14]. A defect of L^{EM} is that it features second-order derivatives of γ, implicitly through the curvature κ, and is thus not directly amenable to global optimization via optimal control methods. Accordingly, an equivalent energy $\mathcal{L}^{\mathrm{EM}}$ is defined using the orientation lifting (2)

$$\mathcal{L}^{\mathrm{EM}}(\mathbf{\Gamma}) = \int_0^1 \psi(\mathbf{\Gamma}(\rho)) \, \mathcal{F}^{\mathrm{EM}}(\mathbf{\Gamma}(\varrho), \mathbf{\Gamma}'(\varrho)) \, d\varrho, \tag{4}$$

[1]The non-vanishing velocity assumption is implicit in the sequel.

where $\mathcal{F}^{\mathrm{EM}} : \mathbb{M} \times \mathbb{E} \to [0, \infty]$ is a Finsler metric defined for any point $\mathbf{x} = (x, \theta) \in \mathbb{M}$ and any non-zero vector $\dot{\mathbf{x}} = (\dot{x}, \dot{\theta}) \in \mathbb{E}$ as follows

$$\mathcal{F}^{\mathrm{EM}}(\mathbf{x}, \dot{\mathbf{x}}) = \begin{cases} \|\dot{x}\| + \frac{\dot{\theta}^2}{\|\dot{x}\|}, & \text{if } \dot{x} \propto \vartheta_\theta, \\ \infty, & \text{otherwise,} \end{cases} \tag{5}$$

where $\vartheta_\theta = (\cos\theta, \sin\theta)^T$ is the unit vector related to $\theta \in \mathbb{S}^1$, and "$\propto$" indicates positive collinearity. The equivalence of $\mathcal{L}^{\mathrm{EM}}$ with L^{EM} follows from the expression (3) of the curvature κ. In order to compute the minimal geodesic curve from a source point $\mathbf{p} \in \mathbb{M}$ to a target point $\mathbf{x} \in \mathbb{M}$, we first estimate a geodesic distance map $\mathcal{D}_{\mathbf{p}} : \mathbb{M} \to [0, \infty)$

$$\mathcal{D}_{\mathbf{p}}(\mathbf{x}) = \inf_{\mathbf{\Gamma}} \Big\{ \mathcal{L}^{\mathrm{EM}}(\mathbf{\Gamma}); \;\; s.t. \; \mathbf{\Gamma}(0) = \mathbf{p}, \; \mathbf{\Gamma}(1) = \mathbf{x} \Big\}.$$

This map is the viscosity solution to an Eikonal equation based on the Hamiltonian $\mathcal{H}^{\mathrm{EM}}$ of the model [34, 42]

$$\mathcal{H}^{\mathrm{EM}}_{\mathbf{x}}(\nabla \mathcal{D}_{\mathbf{p}}(\mathbf{x})) = \tfrac{1}{2}\psi(\mathbf{x})^2, \quad \forall \mathbf{x} \in \mathbb{M} \backslash \{\mathbf{p}\}, \tag{6}$$

with $\mathcal{D}_{\mathbf{p}}(\mathbf{p}) = 0$ and outflow boundary condition on $\partial\mathbb{M}$, where $d\mathcal{D}_{\mathbf{p}}$ is the differential of the geodesic distance map $\mathcal{D}_{\mathbf{p}}$. The Hamiltonian $\mathcal{H}^{\mathrm{EM}}$ is defined from the metric $\mathcal{F}^{\mathrm{EM}}$ by Legendre-Fenchel duality, and has here a closed form

$$\begin{aligned} \mathcal{H}^{\mathrm{EM}}_{\mathbf{x}}(\hat{\mathbf{x}}) &= \sup_{\dot{\mathbf{x}} \in \mathbb{E}} (\langle \hat{\mathbf{x}}, \dot{\mathbf{x}} \rangle - \tfrac{1}{2} \mathcal{F}^{\mathrm{EM}}(\mathbf{x}, \dot{\mathbf{x}})^2) \\ &= \tfrac{1}{8} \Big(\langle \hat{x}, \vartheta_\theta \rangle + \sqrt{\langle \hat{x}, \vartheta_\theta \rangle^2 + \hat{\theta}^2} \Big)^2, \end{aligned} \tag{7}$$

for any base point $\mathbf{x} = (x, \theta) \in \mathbb{M}$ and co-tangent vector $\hat{\mathbf{x}} = (\hat{x}, \hat{\theta}) \in \mathbb{R}^2 \times \mathbb{R}$. An equivalent integral expression of $\mathcal{H}^{\mathrm{EM}}$ can be derived

$$\mathcal{H}^{\mathrm{EM}}_{\mathbf{x}}(\hat{\mathbf{x}}) = \tfrac{3}{8} \int_{-\frac{\pi}{2}}^{\frac{\pi}{2}} \big(\langle \hat{x}, \vartheta_\theta \rangle \cos\varphi + \hat{\theta} \sin\varphi \big)_+^2 \cos\varphi d\varphi. \tag{8}$$

Using the Fejer quadrature rule for integrals, and techniques from discrete geometry, one obtains the approximation [34]

$$\mathcal{H}^{\mathrm{EM}}(\mathbf{x}, \hat{\mathbf{x}}) = \tfrac{1}{2} \sum_{1 \le i \le I} \rho_i^\theta \langle \hat{\mathbf{x}}, \dot{\mathbf{e}}_i^\theta \rangle_+^2 + \|\hat{\mathbf{x}}\|^2 \mathcal{O}(\varepsilon^2), \tag{9}$$

where I is a positive integer, $\rho_i^\theta \ge 0$ is a non-negative weight associated to θ, and $\mathbf{e}_i^\theta \in \mathbb{Z}^3$ is an offset with integer components, for all $1 \le i \le I$. The construction [34]

involves a relaxation parameter $\varepsilon > 0$, chosen in practice as $\varepsilon = 0.1$ with $I = 30$ offsets. A finite differences discretization of the eikonal equation (6), is obtained as a result

$$\sum_{1\leq i\leq I} \rho_i^\theta\Big(\frac{u(\mathbf{x}) - u(\mathbf{x} - h\dot{\mathbf{e}}_i^\theta)}{h}\Big)_+^2 = \psi(\mathbf{x})^2, \qquad (10)$$

with consistency error $\mathcal{O}(h + \varepsilon^2)$, where $h > 0$ is the grid scale. The solution $u \approx \mathcal{D}_{\mathbf{p}}$ is numerically computed using a variant of the FMM [33, 34], see Section 4.1.

Once the geodesic distance map $u \approx \mathcal{D}_{\mathbf{p}}$ is estimated, the geodesic curve $\mathcal{G}$ from the source point $\mathbf{p}$ to an arbitrary target point $\mathbf{x} \in \mathbb{M}$, can be *backtracked*, by solving a simple ODE backwards in time. Namely one sets $\mathcal{G}(T) = \mathbf{x}$, where $T = u(\mathbf{x})$ is the from arrival time, and $\mathcal{G}'(\varrho) = \mathbf{V}(\mathcal{G}(\varrho))$ for all $\varrho \in [0, T]$ where the geodesic flow $\mathbf{V}$ is obtained symbolically and numerically as follows

$$\begin{aligned}\mathbf{V}(\mathbf{x}) &= \frac{d\mathcal{H}^{\mathrm{EM}}_{\mathbf{x}}}{d\hat{\mathbf{x}}}(\nabla\mathcal{D}_{\mathbf{p}}(\mathbf{x})), \qquad (11)\\ &= \sum_{1\leq i\leq I} \rho_i^\theta\Big(\frac{u(\mathbf{x}) - u(\mathbf{x} - h\dot{\mathbf{e}}_i^\theta)}{h}\Big)_+ \mathbf{e}_i^\theta + \mathcal{O}(h).\end{aligned}$$

2.2 Region-based Eikonal Active Contour Model

We briefly review the region-based Eikonal active contour (EAC) model [13, 15], which is used in this paper to build the cost function ψ in Eq. (5). We start from a typical active contour energy comprising of a region-based homogeneity term E_{r} and a regularization term E_{e}

$$E(\mathcal{C}) := \mu E_{\mathrm{r}}(\mathcal{C}) + E_{\mathrm{e}}(\mathcal{C}), \qquad (12)$$

where $\mu \in \mathbb{R}^+$ is a weight parameter and $\mathcal{C} : [0, 1] \to \Omega$ is a closed contour. The component E_{e} is a weighted curve length associated to a Riemannian metric, of the form $E_{\mathrm{e}}(\mathcal{C}) = \int_0^1 \|\mathcal{C}'(\varrho)\|_{\mathcal{M}(\mathcal{C})} d\varrho$. The metric tensor $\mathcal{M}$ is here derived from the image gradients, and such that $\sqrt{\langle\dot{x}, \mathcal{M}(x)\dot{x}\rangle} = \|\dot{x}\|_{\mathcal{M}(x)}$ is low [14] if an edge passes through the point $x \in \Omega$ with tangent $\dot{x} \in \mathbb{R}^2$.

The region-based functional E_{r} measures the homogeneity of image features in each region. In this section, we take the region competition model [48] with the Gaussian mixture model (GMM) as an example to formulate the term E_{r}

$$E_{\mathrm{r}}(\mathcal{C}) = \textstyle\int_{R_1} \xi_1(x)dx + \int_{R_2} \xi_2(x)dx, \qquad (13)$$

where R_1 and R_2 are the regions inside and outside $\mathcal{C}$ respectively, so that $R_1 \cup R_2 = \Omega$. The functions $\xi_i : \Omega \to \mathbb{R}$ measure the image homogeneity within each region R_i. In this paper, we compute each ξ_i using a Gaussian mixture model, for which the probability distribution function (PDF) $P_i(z; \Theta_i)$ are taken as a weighted sum of N Gaussian PDFs. In this case, one has $\xi_i(x) = -\log\big(P_i(f(x); \Theta_i)\big)$, $\forall x \in \Omega$, where Θ_i are the parameters of the GMM and $f : \Omega \to \mathbb{R}^d$ is a gray level image for $d = 1$ or a color image for $d = 3$.

For the EAC model [12, 13, 15], the image segmentation is solved by minimizing the energy (12). A key ingredient for the EAC model is to express, using Stokes theorem, the active contour energy (12) as a weighted curve length. I.e. $E(\mathcal{C}) = \mathcal{L}^{\mathrm{EAC}}(\mathcal{C}) + c$, where c is a constant and where

$$\mathcal{L}^{\mathrm{EAC}}(\mathcal{C}) = \textstyle\int_0^1 \big(\|\mathcal{C}'\|_{\mathcal{M}(\mathcal{C})} + \mu\langle\omega(\mathcal{C}), \mathcal{C}'\rangle\big)d\varrho. \qquad (14)$$

The vector field $\omega : U \to \mathbb{R}^2$ is defined over an open bounded subregion $U \subset \Omega$. As in [12, 15], it is obtained as the solution of the following linear PDE problem

$$\min \int_U \|\omega\|^2 dx, \; s.t. \; \operatorname{curl}\omega(x) = \xi_2(x) - \xi_1(x), \; \forall x \in \Omega.$$

The weighted curve length (14) is an instance of Randers geometry, defined by the non-symmetric metric

$$\mathcal{R}(x, \dot{x}) = \|\dot{x}\|_{\mathcal{M}(x)} + \mu\langle\omega(x), \dot{x}\rangle. \qquad (15)$$

Computing globally optimal minimizers of (14) can be achieved by numerically solving an eikonal equation with Randers anisotropy, leading to a robust minimization procedure for the active contour energy (12) [12, 13, 15].

3 Elastica Curves with Convexity Prior

We present the core contribution: a new elastica geodesic model which can simultaneously take into account the convexity shape prior and curvature regularization, for tracking simple closed and convex geodesic curves.

Definition 1 *A simple closed planar curve γ, smooth and parametrized in* counter-clockwise order*, is said convex iff its curvature κ in Eq. (3) is* non-negative.

3.1 Elastica Metric with Convexity Shape Prior

We introduced in Section 2.1 the Euler-Mumford elastica path length L^{EM}, which we reformulated using orientation lifting (4) and a suitable metric $\mathcal{F}^{\mathrm{EM}}$ in Eq. (5). Globally optimal geodesics can be computed numerically, by solving a generalized Eikonal PDE (6), involving a suitable Hamiltonian (7), using a finite differences scheme (10).

We take here the opposite route, starting from a modified finite differences scheme - which ensures that our approach is practical - all the way back to a variant of the elastica metric embedding the constraint that curvature is non-negative, consistently with Definition 1. The modified scheme reads

$$\sum_{1\leq i\leq I} \tilde{\rho}_i^\theta \Big(\frac{u(\mathbf{x}) - u(\mathbf{x} - h\dot{\mathbf{e}}_i^\theta)}{h} \Big)_+^2 = \psi(\mathbf{x})^2 \qquad (16)$$

where $\tilde{\rho}_i^\theta = \rho_i^\theta$ if $\langle \dot{\mathbf{e}}_i^\theta, (0,0,1) \rangle \geq 0$, and $\tilde{\rho}_i^\theta = 0$ otherwise, for all $1 \leq i \leq I$. Excluding finite differences offsets $\dot{\mathbf{e}}_i^\theta$ whose third component is negative, as we do here and in contrast with the original scheme (10), ensures that the angle θ which is the third component of $\mathbf{x} = (x, \theta) \in \mathbb{R}^2 \times \mathbb{S}^1$ is non-decreasing as the front propagates.

Let us emphasize that the modified finite differences scheme is sufficient to fully implement the numerical method, both the Eikonal solver and the backtracking ODE, by a straightforward adaptation of the geodesic flow (11) (featuring $\mathcal{H}^{\mathrm{C}}$ and $\tilde{\rho}_i^\theta$). The computations below are thus only intended to provide insight on the nature of the PDE that is solved and of the geodesic model that is globally optimized by the method. By construction, comparing with equations (9) and (10), the modified scheme corresponds to the Hamiltonian representation

$$\mathcal{H}^{\mathrm{C}}_{\mathbf{x}}(\hat{\mathbf{x}}) = \tfrac{1}{2} \sum_{1\leq i\leq I} \tilde{\rho}_i^\theta \langle \hat{\mathbf{x}}, \dot{\mathbf{e}}_i^\theta \rangle_+^2 + \|\hat{\mathbf{x}}\|^2 \mathcal{O}(\varepsilon^2), \qquad (17)$$

where $\mathbf{x} = (x, \theta) \in \mathbb{R}^2 \times \mathbb{S}^1$ and $\hat{\mathbf{x}} = (\hat{x}, \hat{\theta}) \in \mathbb{R}^2 \times \mathbb{R}$. An exact integral expression is obtained as $I \to \infty$ and $\varepsilon \to 0$

$$\mathcal{H}^{\mathrm{C}}_{\mathbf{x}}(\hat{\mathbf{x}}) := \tfrac{3}{8} \int_0^{\frac{\pi}{2}} \big(\langle \hat{x}, \vartheta_\theta \rangle \cos\varphi + \hat{\theta} \sin\varphi \big)_+^2 \cos\varphi \, d\varphi. \qquad (18)$$

Note that the proposed integral in Eq. (18) starts at 0, instead of $-\frac{\pi}{2}$ in $\mathcal{H}^{\mathrm{EM}}$. By introducing polar coordinates, one has

$$\mathcal{H}^{\mathrm{C}}_{\mathbf{x}}(\hat{\mathbf{x}}) = r^2 \hbar^{\mathrm{C}}(\phi), \quad \text{with } (\langle \hat{x}, \vartheta_\theta \rangle, \hat{\theta}) = r(\cos\phi, \sin\phi),$$

where $r > 0$ and $\phi \in [-\pi, \pi]$, and where $\hbar^{\mathrm{C}}$ reads as

$$\hbar^{\mathrm{C}}(\phi) := \frac{3}{8} \int_0^{\pi/2} (\cos(\varphi - \phi))_+^2 \cos\varphi \, d\varphi.$$

Distinguishing cases, we obtain a closed form expression of $\hbar^{\mathrm{C}}$, hence also of the modified Hamiltonian $\mathcal{H}^{\mathrm{C}}$, as follows

$$\hbar^{\mathrm{C}}(\phi) = \frac{1}{8} \begin{cases} 0 & \text{if } \phi \in [-\pi, -\frac{\pi}{2}], \\ 2\cos\phi + 2\cos\phi\sin\phi & \text{if } \phi \in [-\frac{\pi}{2}, 0], \\ 1 + \cos^2\phi + 2\cos\phi\sin\phi & \text{if } \phi \in [0, \frac{\pi}{2}], \\ 1 + \cos^2\phi + 2\cos\phi & \text{if } \phi \in [\frac{\pi}{2}, \pi], \end{cases}$$

The metric $\mathcal{F}^{\mathrm{C}}$ of the proposed geodesic model can be expressed in terms of the Hamiltonian $\mathcal{H}^{\mathrm{C}}$ using Legendre-Fenchel duality: $\frac{1}{2}\mathcal{F}^{\mathrm{C}}(\mathbf{x}, \dot{\mathbf{x}})^2 = \max_{\hat{\mathbf{x}}}(\langle \hat{\mathbf{x}}, \dot{\mathbf{x}} \rangle - \mathcal{H}^{\mathrm{C}}(\mathbf{x}, \hat{\mathbf{x}}))$. Considering a non-zero vector $\dot{\mathbf{x}} = (\dot{x}, \dot{\theta}) \in \mathbb{R}^2 \times \mathbb{R}$ and denoting $\dot{s} := \|\dot{x}\|$ one has

$$\mathcal{F}^{\mathrm{C}}(\mathbf{x}, \dot{\mathbf{x}})^2 = \begin{cases} +\infty, & \text{if } \dot{\theta} < 0 \text{ or } \dot{x} \not\propto \vartheta_\theta, \\ (\dot{s} + \dot{\theta}^2/\dot{s})^2, & \text{if } 0 \leq \dot{s} \leq \dot{\theta}, \\ 4(\dot{s}^2 - 2\dot{s}\dot{\theta} + 2\dot{\theta}^2), & \text{if } 0 \leq \dot{\theta} \leq \dot{s} \leq 2\dot{\theta}, \\ \frac{8}{27\dot{\theta}}(9\dot{s}\dot{\theta}^2 + \dot{s}^3 + (\dot{s}^2 - 3\dot{\theta}^2)^{\frac{3}{2}}), & \text{if } 0 \leq 2\dot{\theta} \leq \dot{s}. \end{cases}$$

As expected, the metric $\mathcal{F}^{\mathrm{C}}$ assigns an infinite cost to vectors whose angular velocity component $\dot{\theta}$ is negative. The path length $\mathcal{L}^{\mathrm{C}}$ associated to $\mathcal{F}^{\mathrm{C}}$, similarly to Eq. (4), is thus infinite for curves whose curvature κ takes negative values. Note that $\mathcal{F}^{\mathrm{C}}$ and $\mathcal{F}^{\mathrm{EM}}$ coincide in the regime $0 \leq \dot{s} \leq \dot{\theta}$ which corresponds to a curvature $\kappa = \dot{\theta}/\dot{s} \geq 1$. The set of all $(\dot{s}, \dot{\theta})$ such that $\mathcal{F}^{\mathrm{C}}(\mathbf{x}, (\dot{s}\vartheta_\theta, \dot{\theta})) = 1$, and likewise for $\mathcal{F}^{\mathrm{EM}}$, are illustrated on Fig. 2.

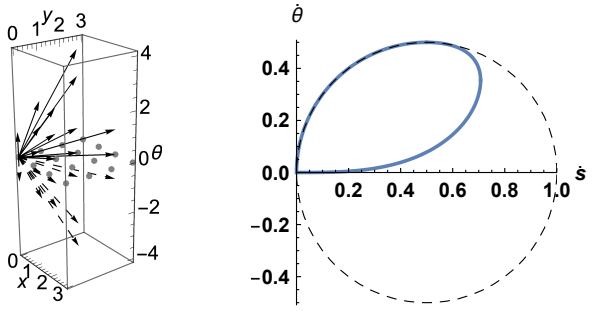

Figure 2: Left: Finite difference stencil of (10) and (16), with dashed arrows when $\langle \dot{\mathbf{e}}_i^{\theta}, (0,0,1)^T \rangle < 0$. Right: Unit vectors in tangent space for the Euler-Mumford elastica model, and the variant with convexity prior constraint. Set of all $(\dot{s}, \dot{\theta})$ such that $\mathcal{F}^{\mathrm{C}}(\mathbf{x}, (\dot{s}\vartheta_\theta, \dot{\theta})) = 1$ (thick solid line), and likewise for $\mathcal{F}^{\mathrm{EM}}$ (dashed line)

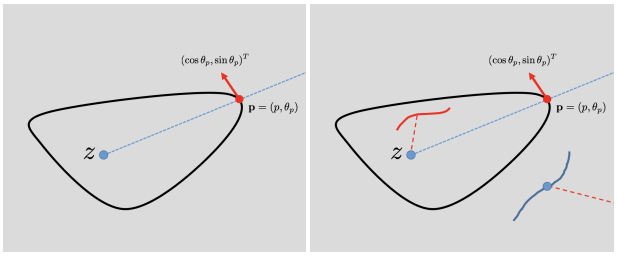

(a) (b)

Figure 3: **a** and **b**: The blue dash line and the red arrows indicate the ray line $\overline{zp}$ and the direction of $(\cos\theta_p, \sin\theta_p)^T$, respectively. The red and blue lines in figure (b) are the scribbles

3.2 Searching Space for Convex Geodesic Curves

The goal is to detect simple and closed convex curves $\mathcal{C}$ to describe target boundaries, whose orientation-lifting $\mathcal{G} = (\mathcal{C}, \eta)$ defined by (2) is a minimizer of the length $\mathcal{L}^{\mathrm{C}}$. For that purpose, we introduce a way of integrating the circular geodesic (CG) model [2] and the total absolute curvature into the computation of geodesic distances associated to the proposed metric $\mathcal{F}^{\mathrm{C}}$. Specifically, the CG method ensures that a *closed* geodesic $\mathcal{G}$ is obtained, while the bound on total absolute curvature eliminates curves whose physical projection $\mathcal{C}$ has *self-intersections*.

The CG Model. At the initialization stage, we exploit two points $\mathbf{p} = (p, \theta_p) \in \Omega \times \mathbb{S}^1$ and $z \in \Omega$ to set up the CG method [2], where p is placed on the boundary of the target region, with tangent orientation θ_p, and z is a point inside the target region. This initialization allows the user to guide the image segmentation in a simple and reliable manner. The ray (half line) originating from z and passing through p is denoted by $\overline{zp} \subset \Omega$. See Fig. 3a, where the angular component θ_p of $\mathbf{p}$ is indicated by the red arrow $(\cos\theta_s, \sin\theta_s)^T$. We consider the following set $\Phi_1(\overline{zp})$, of curves $\gamma : [0,1] \to \Omega$ with C^2-regularity

$$\Phi_1(\overline{zp}) := \left\{\gamma;\ \gamma(0) = \gamma(1) \in \overline{zp},\ \gamma(\varrho) \notin \overline{zp}, \forall \rho \in]0,1[\right\}. \tag{19}$$

Any curve $\gamma \in \Phi_1(\overline{zp})$ is by construction closed and encloses the point z, as illustrated on Fig. 3a, where γ is shown as a black solid line. As discussed in [2], the ray line $\overline{zp}$ is taken as a cut to disconnect the two sides of $\overline{zp}$ in the domain Ω, allowing to efficiently track closed geodesic paths.

Total Curvature. The total curvature $\mathrm{K}(\gamma)$ of a smooth curve $\gamma \in C^2([0,1], \Omega)$ is obtained as

$$\mathrm{K}(\gamma) = \int_0^1 \kappa(\varrho)\, \|\gamma'(\varrho)\|\, d\varrho = \int_0^1 \eta'(\varrho)\, d\varrho, \tag{20}$$

where κ is the curvature (3) and η is the orientation lifting (1). If the curvature κ is non-negative, a property ensured by our geodesic metric $\mathcal{F}^{\mathrm{C}}$ (see Section 3.1), then $\mathrm{K}(\gamma)$ coincides with the *absolute curvature* of γ. We let

$$\Phi_2 := \left\{\gamma \in C^2([0,1], \Omega);\ \mathrm{K}(\gamma) = 2\pi\right\}. \tag{21}$$

Note that $\mathrm{K}(\gamma) \in 2\pi\mathbb{Z}$ when $\gamma : [0,1] \to \Omega$ is a smooth closed curve such that $\gamma'(0) \propto \gamma'(1)$.

Search Space for Geodesic Curves. The search space for geodesic paths, namely simple closed and convex curves, is obtained by combining the constraints of the CG model, of prescribed total absolute curvature, and of non-negative curvature.

Proposition 1 *Consider a smooth curve $\gamma : [0,1] \to \Omega$ with curvature $\kappa : [0,1] \to \mathbb{R}$. Then the curve γ is simple, closed and convex, and encloses the point z, if $\gamma \in \Phi_1(\overline{zp}) \cap \Phi_2$ and $\kappa(\varrho) \geq 0$ for any $\varrho \in [0,1]$.*

The orientation-lifted search space for geodesic paths is defined as

$$\mathbf{\Phi_p} := \{\mathbf{\Gamma} = (\gamma, \eta);\ \gamma \in \Phi_1(\overline{zp}) \cap \Phi_2,\ \mathbf{\Gamma}(0) = \mathbf{\Gamma}(1) = \mathbf{p}\}.$$

Algorithm 1: Geodesic Distances Estimation

Input: A source point $\mathbf{p}$ and the set S_{end}.
Output: Geodesic distance map u.

- Set $u(\mathbf{p}) = 0$ and $u(\mathbf{x}) = \infty$, $\forall x \in \mathbb{M}_h \backslash \{\mathbf{p}\}$.
- Set $\Xi(\mathbf{x}) \leftarrow$ *Trial* and $\hat{\varphi}(\mathbf{x}) = 0$, $\forall x \in \mathbb{M}_h$.
- Construct the neighbourhood $\mathbb{N}$ and set $\mathbf{x}_{\text{m}} \leftarrow \mathbf{p}$.

while $\mathbf{x}_{\text{m}} \notin S_{\text{end}}$ **do**
  Find $\mathbf{x}_{\text{m}}$ minimizing u among all *Trial* points.
  Set $\Xi(\mathbf{x}) \leftarrow$ *Accepted*.
  Update $\tilde{\text{K}}(\mathbf{x}_{\text{m}})$ using the equation (24).
  if $\tilde{\text{K}}(\mathbf{x}_{\text{m}}) \leq 2\pi$ **then**
    foreach $\mathbf{y} \in \tilde{\mathbb{N}}(\mathbf{x}_{\text{m}})$ *s.t.* $\Xi(\mathbf{y}) =$ *Trial* **do**
      Update $u(\mathbf{y})$ by solving the upwind discretization of Eikonal equation (23).
  else
    $u(\mathbf{x}_{\text{m}}) \leftarrow \infty$.

Our numerical method is designed to extract the geodesic curve $\mathcal{G}_{\mathbf{p}}$ which is the global optimum of the problem

$$\mathcal{G}_{\mathbf{p}} = \underset{\boldsymbol{\Gamma} \in \boldsymbol{\Phi}_{\mathbf{p}}}{\arg\min} \left\{ \int_0^1 \psi(\boldsymbol{\Gamma}(\rho))\, \mathcal{F}^{\text{C}}(\boldsymbol{\Gamma}(\varrho), \boldsymbol{\Gamma}'(\varrho))\, d\varrho \right\}. \tag{22}$$

The orientation-lifted curves $\boldsymbol{\Gamma} \in \boldsymbol{\Phi}_{\mathbf{p}}$ with finite energy obey $\mathcal{F}^{\text{C}}(\boldsymbol{\Gamma}(\varrho), \boldsymbol{\Gamma}'(\varrho)) < \infty$, $\forall \varrho \in [0,1]$, which by construction of $\mathcal{F}^{\text{C}}$ implies both the lifting property (1) and the non-negativity of the curvature of γ. The numerical computation of the geodesic path $\mathcal{G}_{\mathbf{p}}$ is presented in Section 4.

Remark. The proposed model allows user to provide scribbles inside and outside the target region. One can randomly choose a point x from an interior scribble, yielding a segment between z and x, which serves as an obstacle together with the scribble such that no curve is allowed to passed through this obstacle. Moreover, each individual exterior scribble and a segment also can yield an obstacle. We can generate a segment linking a point x at this scribble and a point at $\partial\Omega$, where such a segment is supposed to be proportional to the ray line $\overrightarrow{zx}$. As an example, we illustrate these obstacles in Fig. 3b.

4 Numerical Implementation

The Hamilton Fast Marching method (HFM) [33–35] is a state-of-the-art numerical solver of generalized eikonal PDEs. It expects a domain discretized on a Cartesian grid, here $\mathbb{M}_h := (\Omega \cap h\mathbb{Z}^2) \times (h\mathbb{Z} \backslash 2\pi\mathbb{Z})$ a subset of $\mathbb{M} = \Omega \times \mathbb{S}^1$, where $h = 2\pi/N_\theta$ with N_θ being the number of discrete orientations.

4.1 Hamiltonian Fast Marching Solver

Adaptive Stencil Construction. The HFM method takes its name from a specific representation or approximation of the Hamiltonian of the eikonal equation, as a sum of squares of positive parts, similar to Eq. (9) or sometimes slightly more general [33]. Crucially, this representation must only feature non-negative weights, and offsets with integer coordinates, as in Eq. (9). Its design is non-trivial and constitutes the main originality of the method, but is outside the scope of this paper. Depending on the original form of the Hamiltonian, intermediate reformulations may be employed e.g. from (7) to (8), as well as variety of tools from discrete geometry such as Voronoi's first reduction of quadratic forms [35]. This paper differs from previous works [33–35] in the sense that we start from the numerical scheme (16), and derive from it a closed form expression of the Hamiltonian $\mathcal{H}^{\text{C}}$ and metric $\mathcal{F}^{\text{C}}$, see Section 3.1.

The HFM method computes the numerical solution $u : \mathbb{M}_h \to \mathbb{R}$ to the numerical scheme (16) (or likewise (10)), also denoted $u = \mathcal{D}_{\mathbf{p}}$. For that purpose, when adequate, the value $u(\mathbf{x})$ at a point $\mathbf{x} \in \mathbb{M}_h$ is *updated* by solving locally the upwind discretization of the Eikonal equation. In other words, with the notations of (16), we set $u(\mathbf{x}) \leftarrow \lambda$ where

$$\sum_{i \in \mathcal{I}(\mathbf{x})} \tilde{\rho}_i^\theta \, (\lambda - u(\mathbf{y}_i))_+^2 = \psi(\mathbf{x})^2, \quad \text{with } \mathbf{y}_i := \mathbf{x} - h\mathbf{e}_i^\theta, \tag{23}$$

and where $\mathcal{I}(\mathbf{x}) \subset \{1, \cdots, I\}$ is a set of valid indices. Solving for λ in (23) is a straightforward operation also encountered in standard isotropic fast marching. Note that $\mathbf{y}_i$ is a point of the Cartesian grid $h\mathbb{Z}^3$ since the offset $\mathbf{e}_i^\theta$ has integer coordinates, for any $1 \leq i \leq I$. However i is removed from $\mathcal{I}(\mathbf{x})$ under two conditions: (i) if $\mathbf{y}_i$ lies outside the domain $\mathbb{M}_h$, which implements outflow

boundary conditions, and (ii) if the segment $[\mathbf{x}, \mathbf{y}_i]$ intersects[2] the wall $\overline{zp} \times \mathbb{S}^1$, which enforces the closedness condition (19). Point (ii) was developed specifically for the CG model and is one of the contibution of this paper.

We let $\mathbb{N}(\mathbf{x}) := \{\mathbf{y}_i;\, i \in \mathcal{I}(x)\}$ denote the stencil at $\mathbf{x}$, and $\tilde{\mathbb{N}}(\mathbf{x}) := \{\mathbf{y} \in \mathbb{M}_h;\, \mathbf{x} \in \mathbb{N}(\mathbf{y})\}$ the reversed stencil.

Single-pass Distance Estimation Algorithm. At the initialization stage, the HFM tags each grid point $\mathbf{x} \in \mathbb{M}_h$ as *Trial*. We set the geodesic distances $u(\mathbf{x}) = \infty$ for all the grid points $\mathbf{x} \in \mathbb{M}_h \backslash \{\mathbf{p}\}$ and set $u(\mathbf{p}) = 0$ for the source point. During the front propagation, the HFM finds a point $\mathbf{x}_{\rm m}$ which has the smallest distance value among all *Trial* points. This point $\mathbf{x}_{\rm m}$ is immediately tagged as *Accepted*. Then for each point $\mathbf{y} \in \tilde{\mathbb{N}}(\mathbf{x}_{\rm m})$ of the reversed neighborhood, the geodesic distance $u(\mathbf{y})$ is updated by solving the upwind discretization of the Eikonal equation (23), taking only into account the values of geodesic distance map u corresponding to previously *Accepted* points.

Computation of the total absolute curvature. In [21], the authors introduced an efficient method which can simultaneously compute the geodesic distances and the Euclidean distances between the source point $\mathbf{p}$ and any target point $\mathbf{x}$ in an accumulation manner. As a result, the Euclidean length of the geodesic paths can be estimated without backtracking these paths, which reduces computation time. In this paper, we adapt the method of [21] to compute simultaneously the curvature penalized path length $\mathcal{D}_{\mathbf{p}}(\mathbf{x}) = \mathcal{L}^{\rm C}(\mathbf{\Gamma}_{\mathbf{x}})$ of the minimal geodesic $\mathcal{G}_{\mathbf{p},\mathbf{x}} = (\gamma, \eta)$ reaching the point $\mathbf{x}$, *and* its total curvature $\tilde{\rm K}(\mathbf{x})$

$$\tilde{\rm K}(\mathbf{x}) := {\rm K}(\gamma) = \int_0^1 \eta'(\varrho) d\varrho.$$

For that purpose, we note that the total curvature map $\tilde{\rm K}$ obeys a linear PDE, involving the geodesic flow vector field $\mathbf{V} : \mathbb{M} \to \mathbb{R}^2 \times \mathbb{R}$ used in geodesic backtracking (11)

$$\langle \nabla \tilde{K}, \mathbf{V} \rangle = \mathbf{V}_3, \qquad \text{where } \mathbf{V}_3 := \langle (0,0,1)^T, \mathbf{V} \rangle.$$

In addition, the numerical method yields a simple and intrinsic approximation of the geodesic flow (11), of the form $\mathbf{V}(x) = \sum_{i \in \mathcal{I}(x)} \tau_i \dot{\mathbf{e}}_i^{\theta} + \mathcal{O}(h)$ with the notations of (23). Thus one has, using an upwind finite differences scheme

$$\Big(\sum_{i \in \mathcal{I}(x)} \tau_i \Big) \tilde{\rm K}(\mathbf{x}) = \sum_{i \in \mathcal{I}(x)} \tau_i \tilde{\rm K}(\mathbf{y}_i) + h \mathbf{V}_3(\mathbf{x}) + \mathcal{O}(h^2). \tag{24}$$

We solve for $\tilde{\rm K}(\mathbf{x})$ when the point $\mathbf{x}$ is *Accepted*, using this linear equation and omitting the $\mathcal{O}(h^2)$ term. For all $i \in \mathcal{I}(x)$ such that $\tau_i > 0$ one has $\mathcal{D}_{\mathbf{p}}(\mathbf{x}) > \mathcal{D}_{\mathbf{p}}(\mathbf{y}_i)$, hence $\mathbf{y}_i$ was previously *Accepted*. If the value of $\tilde{\rm K}(\mathbf{x}) > 2\pi$, then we set $\mathcal{D}_{\mathbf{p}}(\mathbf{x}) = \infty$ to avoid the self-crossing problem.

In Algorithm 1, we summarize this variant of the HFM for computing the geodesic distance map $u = \mathcal{D}_{\mathbf{p}}$. In order to reduce computation time, the front propagation is terminated when an end point $\mathbf{x}_{\rm e} \in S_{\rm end}$ is tagged as *Accepted*, where the set $S_{\rm end} \subset \mathbb{M}_h$ collects all the immediate grid neighbors of $\mathbf{p} = (p, \theta_p)$ on the correct side of the wall $\overline{zp} \times \mathbb{S}^1$. The desired geodesic path, defined in Eq. (22), is then backtracked following Eq. (11).

Applications to Active Contours. The weighted curve length $\mathcal{L}^{\rm EAC}$ in Eq. (14) can be interpreted in the framework of Section 2.1, by choosing the cost $\psi(x, \theta) = \mathcal{R}(x, \vartheta_\theta)$, and $\beta = 0$. This leads to the possibility of integrating the region-based homogeneity features and curvature regularization for tracking geodesic paths. However, such an interpretation is not what we do in this paper, opt-

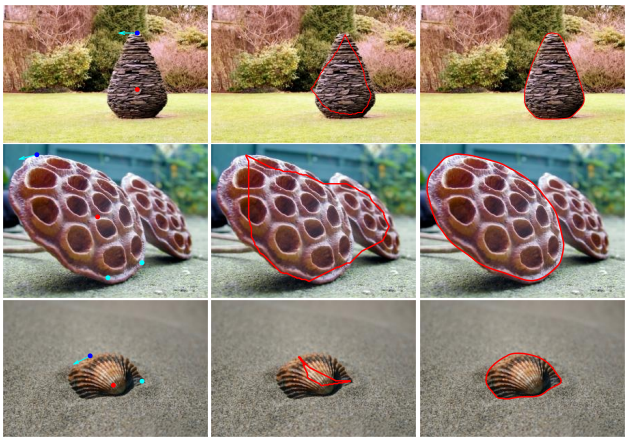

Figure 4: Qualitative comparison with the graph-based model [25]. The original images are shown in column 1. The segmentation results in columns 2 and 3 are derived from [25] and the proposed model, respectively

[2] We allow the intersection between $[\mathbf{x}, \mathbf{y}_i]$ and $\overline{zp} \times \mathbb{S}^1$ in case $\mathbf{x} \in \overline{zp} \times \mathbb{S}^1$ and the vector $\mathbf{y}_i - \mathbf{x}$ points to the left side of $\overline{zp} \times \mathbb{S}^1$.

Figure 5: Qualitative comparison with the EAC model (column 1) and the Euler-Mumford elastica model (column 2). The results in column 3 are derived from the proposed model

ing instead for an exponential cost

$$\psi(x,\theta) = \begin{cases} \exp\big(\alpha \mathcal{R}(x,\vartheta_\theta)\big), & \forall x \in U \\ \infty, & \text{otherwise}, \end{cases} \tag{25}$$

as well as a positive curvature penalty $\beta > 0$. As a result, Stokes theorem does not apply and the equation (4) differs from (12). Nevertheless, this construction of the cost function proves to be very efficient in practice. Note that the subdomain $U \subset \Omega$ should be understood as a search space for geodesic paths such that any geodesic curve $\mathcal{G}_{\mathbf{p}} = (\mathcal{C}_{\mathbf{p}}, \eta_{\mathbf{p}})$ obeys $\mathcal{C}_{\mathbf{p}}(\varrho) \in U, \forall \varrho \in [0,1]$. Up to curve evolution scheme, the goal is to produce sequences $(\mathcal{C}_j)_{j\geq 0}$ of geodesic curves which solve the problem (22), and the subregion U at the j-th iteration is defined as a tubular neighbourhood of $\mathcal{C}_{j-1}$. The initial curve $\mathcal{C}_0$ is required to be simple, closed and convex. Since the edge-based features are independent to the evolving curves $\mathcal{C}_j$. Accordingly, such an admissible initial curve $\mathcal{C}_0$ can be produced using edge-based features only. This can be implemented by simplifying the data-driven velocity $\psi(x,\theta) = \exp(\alpha \|\vartheta_\theta\|_{\mathcal{M}(x)}), \forall x \in \Omega$.

5 Experimental Results

We show the advantages of using convexity shape constraint and curvature regularization in image segmentation, providing that some user interventions are given. In order to configure the proposed geodesic model with convexity shape prior, we need to give the values of α, μ for the data-driven function ψ and of β for controlling the relative importance of the curvature regularization. In the following we set $\alpha \in \{4,5\}$, $\mu \in \{0.1,1\}$ and $\beta \in \{10,20\}$.

In Fig. 4, we illustrate the qualitative comparison results with the graph-based model [25] which features convexity shape prior. The original images sampled from the Weizmann dataset [1] with user-provided points are shown in column 1, where the red and blue dots represent the point z and source point p, respectively. The cyan arrow is positively collinear to $(\cos\theta_p, \sin\theta_p)^T$. The cyan dots are interior points. The foreground seed points for [25] is generated by (i) the segment $[z,s]$, and (ii) the segments between each interior point and z. In addition, the segment linking s and $\partial\Omega$ is taken as the background seed points for [25]. From Fig. 4, we can see that the segmentation results from the proposed model can well capture the desired boundaries of convexity. The segmentation regions from [25] appear to be convex, but fail to depict the targets.

In Fig. 5, we compare the proposed elastica geodesic model to state-of-the-art geodesic models. Specifically, the segmentation results from the EAC model [13,15] and the Euler-Mumford elastica model [14] are respectively depicted in columns 1 and 2. The segmentations from the proposed model are shown in column 3 with initializations, where the cyan star indicates an exterior point. From this figure, one can point out that only the proposed geodesic model integrating convexity shape prior, curvature regularization and region-based homogeneity features are capable of finding suitable segmentation results. In this experiment, all the models are constrained using the identical user input.

We also evaluate quantitative comparisons on 43 CT images sampled from a dataset [43], where the target region of each test image is approximately convex. In order to show the advantages of the proposed model, we add to each CT image Gaussian noise with large standard deviation. We illustrate two examples of these CT images at the bottom of Fig. 6. The quantitative evaluation for the EAC model, the Euler-Mumford elastica model and the proposed model is carried out by the Jaccard Index and the corresponding boxplots are exhibited at the top of Fig. 6. Again, we observe that the proposed model achieves the best performance among the compared approaches. In this experiment, we only exploit the points z

and $\mathbf{p} = (p, \theta_p)$ as initialization. The point z for each test image is taken as the barycentre point of the ground truth region. Each source point p is randomly chosen from the ground truth boundary, while the angular coordinate θ_p is set as the counter-clockwise tangent of the boundary at p.

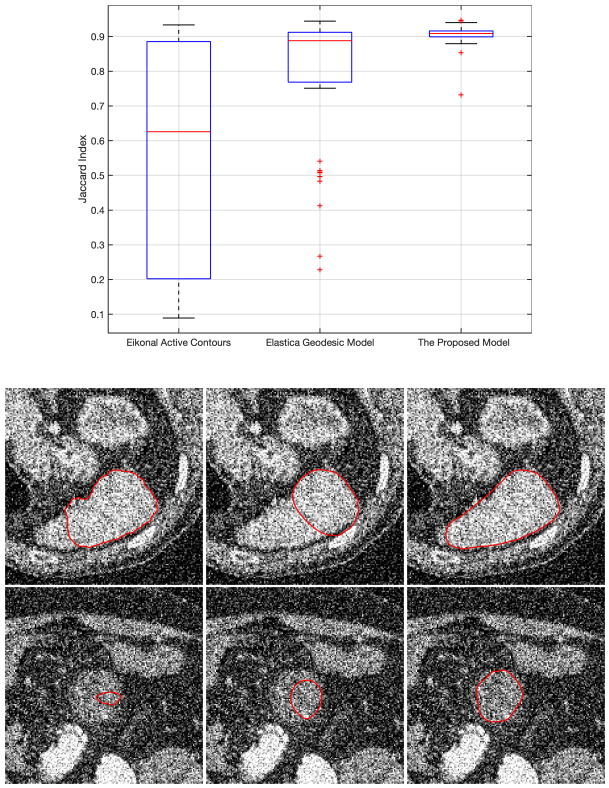

Figure 6: Top: Box plots of the Jaccard index values on 43 CT images with Gaussian noises with respect to the EAC model, the Euler-Mumford elastica model and the proposed one. Bottom: Image segmentations on two typical examples of the used CT images. Columns 1 to 3 correspond to the segmentation results from the EAC model, the Euler-Mumford elastica model and the proposed one, respectively

6 Conclusion

In this paper, we show the possibility of integrating the convexity shape prior, the Euler-Mumford elastica term and the region-based homogeneity image features into the computation of simple and closed geodesic curves. One main contribution lies at the introduction of a variant of the original Euler-Mumford elastica Hamiltonian in order to induce new asymmetric geodesic metrics which encode the convexity shape constraint. As a second contribution, we also introduce efficient numerical solutions for computing convex elastica geodesic curves based on the HFM. Experiments show that the proposed model indeed obtains promising segmentation results.

References

[1] S. Alpert, M. Galun, A. Brandt, and R. Basri. Image segmentation by probabilistic bottom-up aggregation and cue integration. *IEEE Trans. Pattern Anal. Mach. Intell.*, 34(2):315–327, 2012. 10

[2] B. Appleton and H. Talbot. Globally optimal geodesic active contours. *J. Math. Imaging Vis.*, 23(1):67–86, 2005. 7

[3] E. Bae, X.-C. Tai, and Z. Wei. Augmented lagrangian method for an euler's elastica based segmentation model that promotes convex contours. *nverse. Probl. Imaging*, 11(1):1–23, 2017. 2

[4] F. Benmansour and L. D. Cohen. Tubular structure segmentation based on minimal path method and anisotropic enhancement. *Int. J. Comput. Vis.*, 92(2):192–210, 2011. 2

[5] Y. Boykov and G. Funka-Lea. Graph cuts and efficient N-D image segmentation. *Int. J. Comput. Vis.*, 70:109–131, 2006. 2

[6] X. Bresson, P. Vandergheynst, and J.-P. Thiran. A variational model for object segmentation using boundary information and shape prior driven by the Mumford-Shah functional. *Int. J. Comput. Vis.*, 68(2):145–162, 2006. 2

[7] V. Caselles, R. Kimmel, and G. Sapiro. Geodesic active contours. *Int. J. Comput. Vis.*, 22(1):61–79, 1997. 2

[8] T. Chan and W. Zhu. Level set based shape prior segmentation. In *Proc. CVPR*, volume 2, pages 1164–1170. IEEE, 2005. 2

[9] T. F. Chan, S. Esedoglu, and M. Nikolova. Algorithms for finding global minimizers of image segmentation and denoising models. *SIAM J. Appl. Math.*, 66(5):1632–1648, 2006. 2

[10] T. F. Chan, B. Y. Sandberg, and L. A. Vese. Active contours without edges for vector-valued images. *J. Vis. Commun. Image Represent.*, 11(2):130–141, 2000. 2

[11] D. Chen and L. D. Cohen. Fast asymmetric fronts propagation for image segmentation. *J. Math. Imaging Vis.*, 60(6):766–783, 2018. 3

[12] D. Chen and L. D. Cohen. From active contours to minimal geodesic paths: New solutions to active contours problems by Eikonal equations. In *Handbook of Numerical Analysis*, volume 20, pages 233–271. Elsevier, 2019. 2, 5

[13] D. Chen, J.-M. Mirebeau, and L. D. Cohen. Finsler geodesics evolution model for region based active contours. In *Proc. BMVC*, 2016. 2, 5, 10

[14] D. Chen, J.-M. Mirebeau, and L. D. Cohen. Global minimum for a Finsler elastica minimal path approach. *Int. J. Comput. Vis.*, 122(3):458–483, 2017. 3, 4, 5, 10

[15] D. Chen, J.-M. Mirebeau, H. Shu, and L. D. Cohen. Eikonal region-based active contours for image segmentation. *arXiv preprint arXiv:1912.10122*, 2019. 5, 10

[16] D. Chen, J. Spencer, J. M. Mirebeau, K. Chen, and L. D. Cohen. Asymmetric geodesic distance propagation for active contours. In *Proc. BMVC*, 2018. 3

[17] D. Chen, J. Zhang, and L. D. Cohen. Minimal paths for tubular structure segmentation with coherence penalty and adaptive anisotropy. *IEEE Trans. Image Process.*, 28(3):1271–1284, 2019. 2

[18] L. D. Cohen and R. Kimmel. Global minimum for active contour models: A minimal path approach. *Int. J. Comput. Vis.*, 24(1):57–78, 1997. 2

[19] D. Cremers, M. Rousson, and R. Deriche. A review of statistical approaches to level set segmentation: integrating color, texture, motion and shape. *Int. J. Comput. Vis.*, 72(2):195–215, 2007. 2

[20] D. Cremers, F. R. Schmidt, and F. Barthel. Shape priors in variational image segmentation: Convexity, lipschitz continuity and globally optimal solutions. In *Proc. CVPR*, pages 1–6. IEEE, 2008. 2

[21] T. Deschamps and L. D. Cohen. Fast extraction of minimal paths in 3D images and applications to virtual endoscopy. *Med. Image Anal.*, 5(4):281–299, 2001. 9

[22] R. Duits, S. PL Meesters, J.-M. Mirebeau, and J. M Portegies. Optimal paths for variants of the 2D and 3D Reeds–Shepp car with applications in image analysis. *J. Math. Imag. Vis.*, 60(6):816–848, 2018. 3, 4

[23] N. Y. El-Zehiry and L. Grady. Contrast driven elastica for image segmentation. *IEEE Trans. Image Process.*, 25(6):2508–2518, 2016. 2

[24] L. Gorelick and O. Veksler. Multi-object convexity shape prior for segmentation. In *Proc. EMMCVPR*, pages 455–468. Springer, 2017. 2

[25] L. Gorelick, O. Veksler, Y. Boykov, and C. Nieuwenhuis. Convexity shape prior for binary segmentation. *IEEE Trans. Pattern Anal. Mach. Intell.*, 39(2):258–271, 2016. 2, 9, 10

[26] L. Grady. Random walks for image segmentation. *IEEE Trans. Pattern Anal. Mach. Intell.*, 28(11):1768–1783, 2006. 2

[27] V. Gulshan, C. Rother, A. Criminisi, A. Blake, and A. Zisserman. Geodesic star convexity for interactive image segmentation. In *Proc. CVPR*, pages 3129–3136. IEEE, 2010. 2

[28] H. Isack, L. Gorelick, K. Ng, O. Veksler, and Y. Boykov. K-convexity shape priors for segmentation. In *Proc. ECCV*, pages 36–51, 2018. 2

[29] H. Isack, O. Veksler, M. Sonka, and Y. Boykov. Hedgehog shape priors for multi-object segmentation. In *Proc. CVPR*, pages 2434–2442, 2016. 2

[30] R. Kimmel and A. M. Bruckstein. Regularized laplacian zero crossings as optimal edge integrators. *Int. J. Comput. Vis.*, 53(3):225–243, 2003. 2

[31] S. Luo, X.-C. Tai, L. Huo, Y. Wang, and R. Glowinski. Convex shape prior for multi-object segmentation using a single level set function. In *Proc. CVPR*, pages 613–621, 2019. 2

[32] J. Melonakos, E. Pichon, S. Angenent, and A. Tannenbaum. Finsler active contours. *IEEE Trans. Pattern Anal. Mach. Intell.*, 30(3):412–423, 2008. 2

[33] J.-. Mirebeau and J. Portegies. Hamiltonian fast marching: a numerical solver for anisotropic and non-holonomic eikonal PDEs. *Image Processing On Line*, 9:47–93, 2019. 5, 8

[34] J.-M. Mirebeau. Fast-marching methods for curvature penalized shortest paths. *J. Math. Imag. Vis.*, 60(6):784–815, 2018. 2, 3, 4, 5, 8

[35] J.-M. Mirebeau. Riemannian fast-marching on Cartesian grids, using Voronoi's first reduction of quadratic forms. *SIAM J. Numer. Anal.*, 57(6):2608–2655, 2019. 8

[36] D. Mumford and J. Shah. Optimal approximations by piecewise smooth functions and associated variational problems. *Commun. Pure Appl. Math.*, 42(5):577–685, 1989. 2

[37] S. Osher and J. A. Sethian. Fronts propagating with curvature-dependent speed: algorithms based on Hamilton-Jacobi formulations. *J. Comput. Phys.*, 79(1):12–49, 1988. 2

[38] R. Prevost, R. Cuingnet, B. Mory, L. D. Cohen, and R. Ardon. Tagged template deformation. In *Proc. MICCAI*, pages 674–681. Springer, 2014. 2

[39] L. A. Royer, D. L. Richmond, C. Rother, B. Andres, and D. Kainmueller. Convexity shape constraints for image segmentation. In *Proc. CVPR*, pages 402–410, 2016. 2

[40] C. Sagiv, N. A. Sochen, and Y. Y. Zeevi. Integrated active contours for texture segmentation. *IEEE Trans. Image Process.*, 15(6):1633–1646, 2006. 2

[41] T. Schoenemann, F. Kahl, S. Masnou, and D. Cremers. A linear framework for region-based image segmentation and inpainting involving curvature penalization. *Int. J. Comput. Vis.*, 99(1):53–68, 2012. 2

[42] J. A. Sethian and A. Vladimirsky. Ordered upwind methods for static Hamilton–Jacobi equations: Theory and algorithms. *SIAM J. Numer. Anal.*, 41(1):325–363, 2003. 4

[43] J. Spencer, K. Chen, and J. Duan. Parameter-free selective segmentation with convex variational methods. *IEEE Trans. Image Process.*, 28(5):2163–2172, 2019. 10

[44] O. Veksler. Star shape prior for graph-cut image segmentation. In *Proc. ECCV*, pages 454–467. Springer, 2008. 2

[45] S. Yan, X.-C. Tai, J. Liu, and H.-Y. Huang. Convexity shape prior for level set-based image segmentation method. *IEEE Trans. Image Process.*, 29:7141–7152, 2020. 2

[46] C. Yang, X. Shi, D. Yao, and C. Li. A level set method for convexity preserving segmentation of cardiac left ventricle. In *Proc. ICIP*, pages 2159–2163. IEEE, 2017. 2

[47] A. Yezzi, S. Kichenassamy, A. Kumar, P. Olver, and A. Tannenbaum. A geometric snake model for segmentation of medical imagery. *IEEE Trans. Med. Imaging*, 16(2):199–209, 1997. 2

[48] S. Zhu and A. Yuille. Region competition: Unifying snakes, region growing, and Bayes/MDL for multiband image segmentation. *IEEE Trans. Pattern Anal. Mach. Intell.*, 18(9):884–900, 1996. 5